Optimal Feedback Controlled Assembly of Perfect Crystals

Xun Tang,[‡] Bradley Rupp,[†] Yuguang Yang,[†] Tara D. Edwards,[†] Martha A. Grover,[*,‡] and Michael A. Bevan[*,†]

[‡]School of Chemical & Biomolecular Engineering, Georgia Institute of Technology, Atlanta, Georgia 30332, United States
[†]Department of Chemical & Biomolecular Engineering, Johns Hopkins University, Baltimore, Maryland 21218, United States

ⓢ *Supporting Information*

ABSTRACT: Perfectly ordered states are targets in diverse molecular to microscale systems involving, for example, atomic clusters, protein folding, protein crystallization, nanoparticle superlattices, and colloidal crystals. However, there is no obvious approach to control the assembly of perfectly ordered global free energy minimum structures; near-equilibrium assembly is impractically slow, and faster out-of-equilibrium processes generally terminate in defective states. Here, we demonstrate the rapid and robust assembly of perfect crystals by navigating kinetic bottlenecks using closed-loop control of electric field mediated crystallization of colloidal particles. An optimal policy is computed with dynamic programming using a reaction coordinate based dynamic model. By tracking real-time stochastic particle configurations and adjusting applied fields *via* feedback, the evolution of unassembled particles is guided through polycrystalline states into single domain crystals. This approach to controlling the assembly of a target structure is based on general principles that make it applicable to a broad range of processes from nano- to microscales (where tuning a global thermodynamic variable yields temporal control over thermal sampling of different states *via* their relative free energies).

KEYWORDS: *colloidal assembly, low dimensional models, energy landscapes, stochastic ensemble control, Markov decision process*
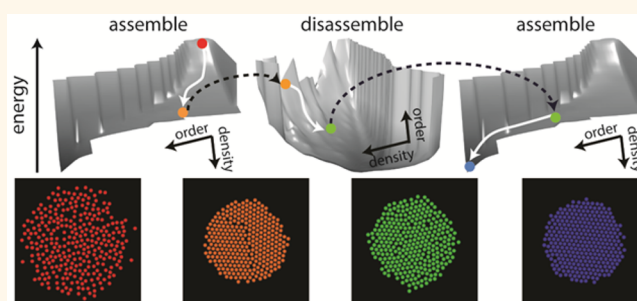
Assembling colloidal nano- and microparticle components into perfectly ordered configurations could enable metamaterials with exotic properties that are otherwise unattainable.[1−4] Obtaining perfect structures is nontrivial at any scale (*e.g.*, atomic clusters, nanoparticle superlattices, folded proteins). Limited successful examples of perfect crystals on molecular scales include monocrystalline silicon for microelectronics *via* near-equilibrium directional growth from a seed crystal and single small protein crystals for X-ray crystallography *via* combinatorial screening. Such perfect atomic and molecular crystals are often obtained using open-loop control at near equilibrium conditions; that is, recipes based on slow nucleation, growth, and annealing to allow constituents to gradually assemble and relax into global free energy minimum perfect crystals. Like molecular crystallization, the capability to tune colloidal nano- and microparticle crystallization has been shown in a number of studies;[5−17] however, the controlled assembly of perfect thermodynamically stable colloidal crystals has not yet been demonstrated.

Crystallization kinetics depends on how constituents collectively assemble *via* diffusion. Molecular diffusion rates allow crystal growth near equilibrium to occur on time scales that are economically viable for manufacturing of high value-added materials. Colloidal nano- to microscale components, by virtue of their size, diffuse orders of magnitude more slowly than molecules, and hence colloidal assembly at near equilibrium conditions is impractical. The alternative, rapid out-of-equilibrium assembly, leads to defects (*e.g.*, polycrystals) and often arrested amorphous states. There appears to be an insurmountable gap between the limits of assembling perfect crystals *via* excessively long equilibrium processes and rapidly producing defective structures.

Here, we overcome the inherent drawbacks of open-loop controlled colloidal particle assembly processes by demonstrating rapid assembly of perfect crystals with closed-loop ("feedback") control based on a microscopic dynamic model. Practically, the experiment involves compressing charged colloids within a quadrupolar electric field (Figure 1). This is a self-assembly process in which a global thermodynamic variable (*i.e.*, electric field) changes the relative free energy of all configurations, causing particles to assemble *via* thermal motion to minimize their free energy. To enable feedback control,
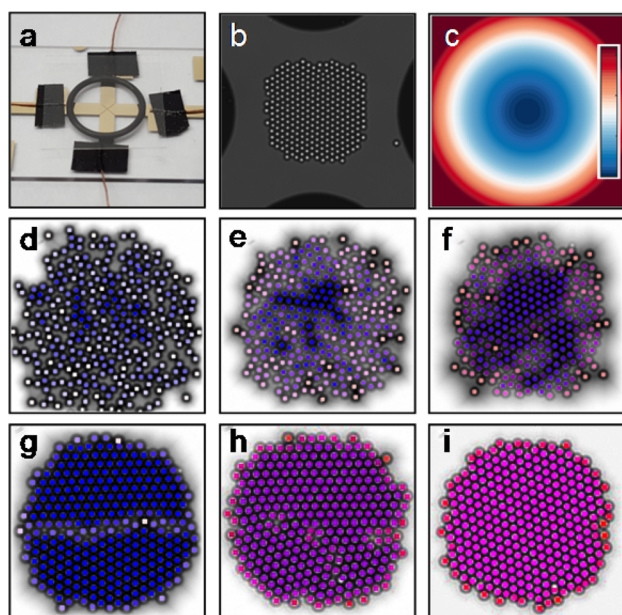
Figure 1. Quasi-2D colloidal crystal assembly in electric fields. (a) Microfabricated quadrupole electrode. (b) Optical microscopy image of particles within quadrupole. (c) Single particle-field potential (blue−red scale: 0−100kT). Images of 300 particles with centers colored to visualize reaction coordinates for local hexagonal order, C_6, and global hexagonal order, ψ_6, at electric field amplitudes of λ = (d) 0.2, (e) 0.9, (f) 2.0, and (g, h, i) 19.7. Representative microstructures include bicrystals with (g) large grain boundary (similar sized domains near max misorientation angle), (h) small grain boundary (dissimilar sized domains with smaller misorientation angle), and (i) no grain boundary, that is, perfect crystal. The 2.8 μm particles provide an internal scale bar.

essential real-time capabilities require (1) sensing the system state (*via* image analysis), (2) actuating particle interactions to navigate energy landscapes (*via* field mediated potentials), and (3) closing the loop to assign actuator settings based on sensor readings (*via* an optimal policy). This approach corrects defects in real-time to produce perfect crystals. While feedback control has been explored in microscopic systems including single particles,[18] colloidal assembly,[19] shear induced transitions,[20] nanostructure morphology,[21] and maximizing crystallinity,[22] none have produced perfect crystals using real-time defect correction.

Ultimately, this study is a proof-of-principle demonstration of controlling the navigation between two states in free energy space,[23] which we practically implement to create perfect 2D colloidal crystals. However, this approach could be used to navigate between any states including other colloidal microstructures (*e.g.*, gels, glasses, chains, clusters). Because colloidal particles thermally sample different configurations *via* diffusion based on their relative free energies and as such are often considered as models of atoms[24−26] (often in connection to the thermodynamics and kinetics of crystallization),[27−31] the physics underlying our approach is general across a range of length scales including molecular and nanoscales. As such, if correctly adapted (including appropriate methods to tune interactions[5−9] and to sense states, *e.g.*, *via* diffraction,[32,33] optical Fourier transforms,[34] super-resolution microscopy,[35,36] liquid cell electron microscopy[37]), the approach outlined in this work could be used to control states in systems of atoms, molecules, macromolecules, and nanoparticles. In addition to

enabling the assembly of static, equilibrium target states, the ability to actively control particle ensembles between different nonequilibrium states could enable reconfigurable metamaterials (*i.e.*, metadevices).[38]

RESULTS AND DISCUSSION

Stochastic Polycrystal Assembly. Assembly is performed with 300 SiO$_2$ colloids (radius, a = 1.4 μm) confined by gravity into a quasi-2D layer within a quadrupole electrode (Figure 1a, see Methods and Supporting Information (SI)). A function generator controls the amplitude of a 1 MHz AC field, which determines the degree of localization of colloids at the field minimum in the quadrupole center (Figure 1b). The dipole-field potential characterizing the potential energy associated with confining particles is (Figure 1c)[39]

$$u(\mathbf{r}) = -\lambda f_{CM}^{-1}[E(\mathbf{r})/E_0]^2 \tag{1}$$

where $\lambda = \pi_m a^3 (f_{CM} E_0)^2/(kT)$ characterizes how strongly the radially varying field, $E(r)/E_0$, confines particles relative to thermal energy, kT, and f_{CM} depends on the particle, ε_p, and medium, ε_m, dielectric properties (see Methods and SI).[40] A balance of the field confinement against the quasi-2D dispersion osmotic pressure determines, for a given particle number, whether a fluid or solid phase will form *versus* λ (Figure 1d−i).[41] As system size increases, polycrystallinity (*i.e.*, misoriented crystal domains with grain boundaries, Figure 1g,h) becomes increasingly prevalent; this is the defect we aim to repair *via* feedback control.

To develop a sensor and model for grain boundary formation and motion, we employ a reaction coordinate based dynamic model.[42] Two reaction coordinates are necessary to quantify polycrystallinity: the degrees of global order, ψ_6, and local order, C_6. Values of ψ_6 and C_6 are computed in real-time from particle centers obtained *via* microscopy and image analysis (see Methods and SI). To briefly describe how reaction coordinates capture different states, $\psi_6 \approx 0$ for amorphous states (Figure 1d) and polycrystals (Figure 1g), whereas $\psi_6 \approx 1$ for perfect crystals (Figure 1h). C_6 captures the emergence of crystallinity during condensation and distinguishes amorphous (low C_6) and polycrystalline (high C_6) states (which both have $\psi_6 \approx 0$).

Polycrystallinity *versus* Uncontrolled Ramp Rate. We illustrate the need for feedback control by first showing examples without feedback control that demonstrate the trade-off between generating perfect crystals *via* slow, near-equilibrium ramps *versus* polycrystals *via* ramps too fast for relaxation into single crystals (Figure 2). Assembly trajectories are reported for N = 300 particles in Brownian Dynamic (BD) simulations matched to experiments[42] for several orders of magnitude in field ramp time. Nonequilibrium ψ_6 and C_6 trajectories averaged over 100 simulations for ramp times of 0, 1 × 10^3, 2 × 10^3, 5 × 10^3, and 10^4 s are shown alongside equilibrium ψ_6 (*i.e.*, free energy minima values at each λ, see SI). As expected, local ordering always precedes global ordering. The key result is that a ramp time greater than 10^4 s is required to achieve 100% perfect crystals in the near-equilibrium limit (*i.e.*, ramped ψ_6 passes through equilibrium ψ_6 values at long times). Faster ramps produce nonequilibrium polycrystals that do not relax to single crystals in the allotted times.

Feedback Controlled Navigation of Energy Landscapes. The (ψ_6, C_6) coordinates quantitatively capture nonequilibrium stochastic trajectories between states, which
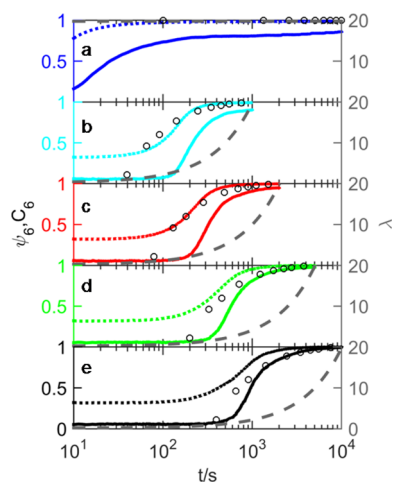
Figure 2. Ramping electric field at different rates without feedback control to understand effect of quench-rate on crystal assembly. Electric field amplitude, λ (long-dash gray), ramped from 0.2 to 19.7 over (a) 0 s (blue), (b) 1×10^3 s (cyan), (c) 2×10^3 s (red), (d) 5×10^3 s (green), and (e) 10^4 s (black). Local order, C_6 (dotted lines), emerges before global order, ψ_6 (solid lines). Equilibrium ψ_6 values (open circles) vs λ approach ψ_6 ramp trajectories only for the 10^4 s ramp.

provides a dynamic model to *close the loop* between *sensing* (determining the current state) and *actuation* (specifying λ to achieve a new state). A (ψ_6, C_6) based model quantifies field mediated crystallization dynamics *via* a Smoluchowski equation given as[42]

$$\frac{\partial p(\mathbf{x}, \lambda, t)}{\partial t} = \nabla \cdot \mathbf{D}(\mathbf{x}, \lambda) \cdot \left[\nabla + \frac{1}{kT} \nabla W(\mathbf{x}, \lambda) \right] p(\mathbf{x}, \lambda, t)$$

(2)

where p is probability, $\mathbf{x} = (\psi_6, C_6)$, $\mathbf{D}$ is a diffusivity landscape, and W is a free energy landscape. The dynamic model encapsulated in eq 2 enables formulating an optimal control scheme based on free energy gradients in W and hydrodynamic mediated friction in $\mathbf{D}$.[42]

Controlling crystallization is conceptually the navigation of free energy landscapes, W, at each electric field amplitude, λ (Figure 3a). The equilibrium ramp (Figure 2e) corresponds to slowly increasing $\lambda(t)$ so the configuration resides near the free energy minimum on each W. Faster ramps (Figure 2a−d) in $\lambda(t)$ cause sampling of nonequilibrium polycrystalline states on each W where vanishing gradients provide minimal driving force for relaxation.[42] The more sophisticated approach here is to determine the optimal $\lambda(t)$ based on current (ψ_6, C_6) coordinates to maximize the probability of moving from the initial fluid to the perfect crystal. Because the particle and grain boundary motion are stochastic, each process is unique, so no one $\lambda(t)$ is best every time; instead closed-loop control is required to obtain the optimal actuation.

To determine how to change the electric field *versus* time (*i.e.*, $\lambda(t)$) to best navigate the free energy landscapes, W, we use a Markov decision process based policy using dynamic programming.[43] This framework requires a discretized version of eq 2, known as a Markov state model,[44] which consists of a "probability transition matrix" to quantify the transition probability between all states during a time step, Δt, at each λ. The resulting policy, π, provides a mapping from the current measured state, $\mathbf{x}$, to the next action, λ, to be taken. Mathematically, $\lambda_{i+1} = \pi(\mathbf{x}_i)$, where i is the time step. The
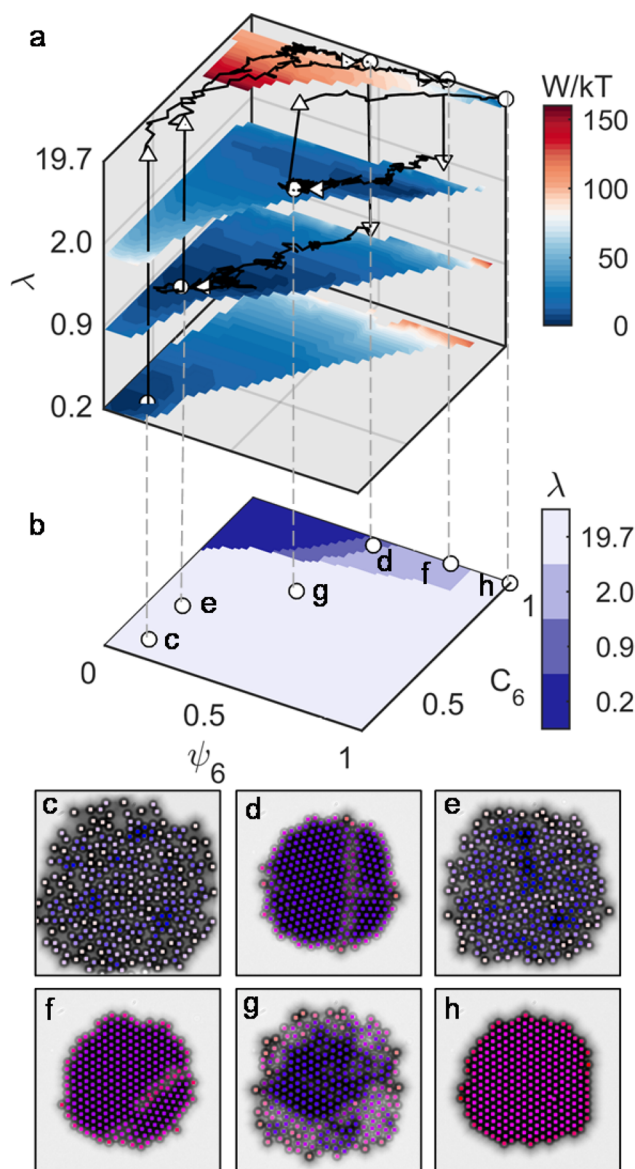

Figure 3. Assembly trajectory on energy landscapes under control (see Movie S1). (a) Free energy landscapes of 300 particles at the four λ's in policy. Example trajectory (black) with coordinates on policy (b) and corresponding images (c−h). (b) Optimal policy calculated using Markov decision process. Images showing representative configurations (same coloring scheme as Figure 1d−i) at (c) $\lambda = 0.2$ before compression, (d) first compression to $\lambda = 19.7$ with grain boundary, (e) relaxation at $\lambda = 0.9$, (f) recompression at $\lambda = 19.7$ with new grain boundary, (g) relaxation at $\lambda = 2.0$, and (h) perfect crystal at $\lambda = 19.7$.

optimal policy at each state $\mathbf{x}$ maximizes the objective function J^π,[45]

$$J^\pi(\mathbf{x}) = X \left\{ \sum_{i=0}^{\infty} \gamma^i R(\mathbf{x}_i, \lambda_i) \right\}$$

(3)

where X is the expectation operator and $R(\mathbf{x}_i, \lambda_i)$ is the reward function at time step i. In this work, $R = \psi_6^2$, such that a high global crystallinity is "rewarded". The discount factor γ ensures convergence of the policy calculation, and here is set to 0.99 (see Methods for details). The Markov decision process calculation provides the optimal policy (Figure 3b) in the form

of a look-up table, indicating the λ to use when assembly trajectories pass through each (ψ_6, C_6) coordinate.

A typical single experimental trajectory (Figure 3a,b) illustrates how the control policy is implemented. Practically, the feedback control is achieved in real-time via the following steps: (1) image analysis is used to locate particle centers and compute updated (ψ_6, C_6) coordinates every 100 ms, which are plotted as trajectories on the W at each λ (Figure 3a); (2) the current values of the (ψ_6, C_6) coordinates are found in the optimal control policy look-up table (Figure 3b); and (3) the new value of the quadrupole voltage (λ) found in the look-up table is updated every 100 s, which is shown by the trajectories jumping between the W in Figure 3a every time the λ value is changed. The policy update time of $\Delta t = 100$ s was determined by considering actuation times comparable to the inherent system response time.

The policy update time and inherent system response time depends on the cooperative short-range motion of particles necessary for grain boundary motion,[46,47] which can be estimated from the long time self-diffusivity as, $D_S^L = D_S^S[1 + 2\phi g(2a)]^{-1}$, where D_S^S is the short time self-diffusivity, ϕ is the particle area fraction, and $g(2a)$ is the radial distribution function contact value within the quasi-2D colloidal mono-layer.[48] Using $D_S^S = 0.5D_0$ (D_0 is the Stokes−Einstein value) to account for particle-wall hydrodynamics,[49] and the hard disk fluid radial distribution function for $g(2a)$,[50] the time for particles to diffuse over a distance comparable to their own radius is $\tau = a^2/D_S^L \approx 100$ s at low concentrations. By considering how the soft electrostatic repulsion between particles significantly decreases $g(2a)$,[48] D_S^L becomes a weak function of ϕ, and as such, $\tau \approx 100$ s captures the characteristic structure relaxation time scale for all configurations and λ. Estimating D_S^L based on dense fluid properties can be rationalized since motion within grain boundaries has been compared to concentrated melt dynamics.[31,51,52] In addition, the different λ values in conjunction with the inhomogeneous field cause the dynamics to vary significantly from the concentrated interior of the particle ensemble to the vanishing density at its periphery.[41] Practically, the 100 s update time worked better than faster or slower times, consistent with the above analysis.

Movies (Movie S1) and images of particle configurations (Figures 3c−h) at start, end, and policy update points (Figure 3b) show that the policy uses (1) the highest field ($\lambda = 19.7$) for rapid initial assembly and to quench the final perfect crystal, (2) the lowest field ($\lambda = 0.2$) to partially disassemble large grain boundaries, and (3) intermediate field amplitudes ($\lambda = 0.9$, $\lambda = 2.0$) to assist relaxation of smaller grain boundaries. The control policy at most times drives rapid assembly at the highest field setting and is only reduced occasionally to eliminate defects without completely disassembling structures and restarting assembly.

Controlled *versus* Uncontrolled Assembly. Because colloidal assembly trajectories are stochastic, it is essential to collect sufficient statistics for a fair comparison of uncontrolled and controlled processes; to address this issue, 200 alternating uncontrolled and controlled cycles were obtained in a fully automated experiment over >31 h (see Methods and SI, Figure 4). Each cycle used feedback control to: (1) ensure initial disassembly, (2) execute either a step-quench without intervention or a series of 100 s control updates, and (3) terminate the process after either obtaining a perfect crystal or a period of 10^3 s. The first 10 cycles illustrate several scenarios
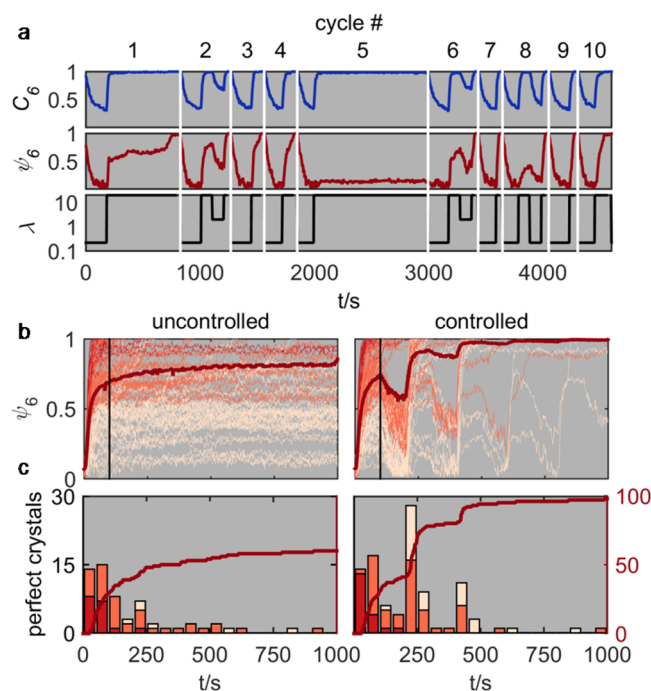

Figure 4. Controlled *vs* uncontrolled crystal assembly processes: 100 uncontrolled and 100 controlled trajectories shown as (a) first 10 cycles with C_6 (blue), ψ_6 (red), and λ (black) *vs* time, (b) ψ_6 *vs* time for 10^3 s for all experiments colored to indicate ensemble average (bold red), no grain boundary (red, $\psi_6 > 0.7$, $C_6 > 0.95$), small grain boundary (orange, $0.7 > \psi_6 > 0.4$, $C_6 > 0.95$), and large grain boundary (peach, $0.4 > \psi_6$, $C_6 > 0.95$), and (c) perfect crystals *vs* time as cumulative number (dark red) and instantaneous number (bars) with same color scheme as panel b.

(Movie S2, Figure 4a) including trajectories that (1) quickly relax for small grain boundaries (#3, #7, #9), (2) slowly relax to form a perfect crystal in <1000 s (#1), (3) form metastable crystals that never relax (#5), and (4) always form perfect crystals either without (#4, #10) or with (#2, #6, #8) several feedback corrections.

Analysis of all 200 ψ_6 versus time trajectories (Figure 4b) and number of perfect crystals *versus* time (Figure 4c) show key quantities to assess the controller's success at producing perfect crystals. A handful of perfect crystals form immediately during coalescence without grain boundaries (17 uncontrolled *vs* 19 controlled) by bypassing slow grain boundary motion on free energy plateaus (W at $\lambda = 19.7$ in Figure 3a).[42] The remaining ∼160 trajectories illustrate how control removes grain boundaries by choosing lower λ. When removing small grain boundaries, perfect crystals are obtained in 100% (52/52) of trajectories after 1−2 corrective steps, whereas 78% (37/47) of small grain boundary bicrystals relax to perfect crystals without control. The ultimate test of the controller is for large grain boundaries; 93% (27/29) of controlled trajectories produce perfect crystals after 3−4 corrective steps *vs* 18% (6/34) of uncontrolled processes. In the final accounting, controlled processes produced perfect crystals 98% of the time, while uncontrolled processes were 60% successful.

CONCLUSIONS AND OUTLOOK

Our results demonstrate optimal feedback control to robustly assemble perfect colloidal crystals orders of magnitude faster than a slow quasi-equilibrium ramp and much more reliably

than rapid quenches. An optimal policy is computed with dynamic programming based on a low-dimensional reaction coordinate dynamic model. By tracking real-time stochastic particle configurations and employing the optimal policy to adjust applied electric fields *via* feedback, the evolution of unassembled particles is guided through polycrystal states into single domain crystals.

There are a number of ways this approach could be adapted and extended. For example, our approach could be implemented to constructively employ multiple complementary actuators (*e.g.*, magnetic fields to exert torques,[53] tunable depletion attraction to quench final states)[54] or be combined with other methods such as templated self-assembly (either unactuated[55,56] or actuatable[57]). Based on our prior work on nanoparticle assembly,[58] system size effects,[41] and three-dimensional assembly in electric[59] and gravitational fields,[60] our approach can also be adapted to (1) smaller nanoparticles (with different sensors; *e.g.*, attenuation based imaging,[58,60] scattering/diffraction),[32] (2) larger systems either through continuous processing (rather than batch processing; *e.g.*, a microfluidic device), parallelization (*e.g.*, electrode arrays),[61] or informing open-loop schemes (*e.g.*, toggling),[16] and (3) 3D crystals in thin films and possibly bulk crystals.

Further extensions of the methods and analyses developed in this work could be applied to other nano- and microscale processes involving anisotropic particles or multicomponent mixtures (with more states and bottlenecks), dynamical steady-states and out-of-equilibrium end points (where a Fokker–Planck equation describes the dynamics rather than a Smoluchowski equation), active micromachines and reconfigurable device elements (rather than static targets), and even synthetic materials systems that mimic basic control elements in biological systems (*e.g.*, chaperone control of protein folding and aggregation).[62] Our approach is based on first-principle concepts that are general to any molecular, nano-, or microscale assembly process where components thermally sample different configurations based on their relative free energies, states can be measured in real-time, an actuation mechanism exists to alter driving forces, and a dynamic model connects system responses to actuator settings.

METHODS

Sample Preparation. Coplanar quadrupole Au thin film electrodes were patterned on glass microscope coverslips that were sonicated in acetone for 30 min, sonicated in isopropanol (IPA) for 30 min, rinsed with deionized (DI) water, soaked in Nochromix (Godax) for 1 h, rinsed with DI water, sonicated in 0.1 M KOH for 30 min, rinsed with DI water, and dried with N_2. The electrodes were fabricated by spin coating photoresist (S1813, Shipley) onto microscope coverslips, UV exposure through a chrome photomask, and physical vapor deposition of a 15 nm chromium adhesive layer and a 35 nm gold layer. The photoresist liftoff was accomplished with agitation in 1165 Remover (Shipley). The electrode tips are separated by ~100 μm. Prior to experimentation, the coverslips with patterned quadrupole electrodes were sonicated in IPA for 30 min, acetone for 30 min, and IPA for 30 min, rinsed in DI water, then suspended in Nochromix for 20 min, rinsed with DI water, and dried with N_2.

Experiments were performed in batch cells consisting of Viton O-rings. To construct batch cells, O-rings were coated with vacuum grease and sealed between the coverslip with the electrode and a glass coverslip. Colloidal particle dispersion (100 μL) was dispensed into the batch cell and allowed to sediment for 5 min prior to sealing with a coverslip to obtain approximately 300 particles in the quadrupole. Twenty-two gauge copper wires were attached to the electrode using conductive carbon tape. The electrode was then connected in series

with a function generator (Agilent 33220a) with one lead attached to the north–south poles and another to the east–west poles.

Microscopy. Microscopy was performed on an inverted optical microscope with a 63× Zeiss air objective lens (0.6 numerical aperture) at 1.25 magnification. A 12-bit CCD camera captured 336 pixel × 256 pixel (104 μm × 79 μm) digital images at rate of 10 frames/s. Image capture and analysis were performed using MATLAB Image Processing and Image Acquisition Toolboxes. Image analysis algorithms coded in MATLAB were used to simultaneously locate and track particle centers, as well as compute local and global order parameters in real time,[19] Experimental values of ψ_6 and C_6 were normalized by constants $\psi_{6,max} = 0.8$ and $C_{6,max} = 0.95$ to account for particle tracking errors.

Feedback Control. The electric field amplitude and frequency were controlled *via* the function generator using a device driver written in the MATLAB Instrument Control Toolbox. A sinusoidal voltage with a 1 MHz frequency was varied among $\lambda = 0.2, 0.9, 2.0$, and 19.7 for controlled cycles and held at a constant $\lambda = 19.7$ for uncontrolled cycles. The value of λ is related to the electric field and peak to peak voltage as

$$\lambda = \pi \varepsilon_m a^3 (f_{CM} E_0)^2 / (kT) \qquad E_0 = 8^{-0.5} V_{pp}/d_g \qquad (4)$$

where λ has the same definition as the main manuscript, d_g is the electrode gap, and V_{pp} is the peak-to-peak voltage set in the function generator. For $d_g = 100$ μm in this and previous work, the value of V_{pp} at which all particles crystallize in a system of N particles was determined to be

$$V_{pp} = a_0 N^{-b_0} \qquad a_0 = 7.15 + 4.10 \times 10^{-3} \kappa^{-1}$$
$$b_0 = 0.219 + 4.24 \times 10^{-4} \kappa^{-1} \qquad (5)$$

where κ^{-1} is the Debye length. Values of V_{pp} and λ used in this work are reported in Supplementary Table 1.

Several properties could change in the course of a ~31 h experiment, such as particle stability, solvent conditions, and evaporation. However, there is no evidence that any of these factors changed the experimental conditions by plotting any measured quantity *versus* time. This is shown by the fact that the probability that an uncontrolled cycle would form a perfect crystal remains for all practical purposes constant for the experiment duration.

The radius of gyration, R_g, was used to measure the degree of melting between individual cycles. After a perfect crystal was obtained or 1000 s had elapsed, the system was melted at $\lambda = 0.2$ until $R_g = 25.5$ μm, at which point the next crystallization cycle was started. R_g is given by

$$R_g = 0.5 N^{-1} \left[\sum |r_i - r_j|^2 \right]^{0.5} / R_{g,HEX} \qquad (6)$$

where $R_{g,HEX}$ is the radius of gyration for two-dimensional hexagonally close packed particles with regular polygon morphologies given by

$$R_{g,HEX} = 5^{0.5} 3^{-1} a N^{0.5} \qquad (7)$$

Reaction Coordinates. Reaction coordinates are computed for different system sizes to include edge effects. The global 6-fold bond orientational order, ψ_6, is given by[54,63,64]

$$\psi_6 = \left| \frac{1}{N} \sum_{j=1}^{N} \psi_{6,j} \right| \qquad (8)$$

where N is the total number of particles in the ensemble, and $\psi_{6,j}$ is the local 6-fold bond orientation order of particle j given as

$$\psi_{6,j} = \frac{1}{N_{C,j}} \sum_{k=1}^{N_{C,j}} e^{i6\theta_{jk}} \qquad (9)$$

where $N_{C,j}$ is the number of neighbors within the first $g(r)$ peak (coordination radius) of particle j, and θ_{jk} is the angle between particle j and each neighboring particle k with an arbitrary reference direction. Connectivity between crystalline particles, $\chi_{6,jk}$, is given by

$$\chi_{6,jk} = \frac{|\mathrm{Re}[\psi_{6,j}\psi_{6,k}^*]|}{|\psi_{6,j}\psi_{6,k}^*|} \tag{10}$$

where $\psi_{6,j}^*$ is the complex conjugate of $\psi_{6,j}$. This is used to compute the local order parameter for 6-fold connectivity, $C_{6,j}$, which produces integer values between zero and six. The number of crystalline nearest neighbors, $C_{6,j}$, for particle j is determined using the criterion[65]

$$C_{6,j} = \sum_{k=1}^{N_{C,j}} \left[\begin{matrix} 1 & \chi_{6,jk} \geq 0.32 \\ 0 & \chi_{6,jk} < 0.32 \end{matrix} \right] \tag{11}$$

$$C_6 = \frac{1}{N} \sum_{i=1}^{N} C_{6,i} / \langle C_6 \rangle_{\mathrm{HEX}} \tag{12}$$

where C_6 is the average normalized local 6-fold connectivity, normalized by $\langle C_6 \rangle_{\mathrm{HEX}}$, the C_6 value for 2D hexagonal close packed particles with a hexagonal morphology given by[19]

$$\langle C_6 \rangle_{\mathrm{HEX}} = N^{-1}6(3S^2 + S) \tag{13}$$

$$S = -(1/2) + [(1/3)(N-1) + (1/4)]^{1/2} \tag{14}$$

Markov State Model Construction. A Markov state model (MSM)[44] is characterized by a set of discretized states S, and a probability transition matrix $P(\lambda)$ for each input λ. $P(\lambda)$ is composed of transition probability $P(\lambda)_{ij}$, which denotes the probability of the system to be in state j after a transition time of Δt given the current state as i under an input λ. The state space is defined by the reaction coordinates (ψ_6, C_6). The discretization is fine enough to distinguish configurations that lead to different dynamics but not too fine to lead to sampling issues in building the transition matrix and computational issues in solving for the control policy.[66] We discretized the reaction coordinate ψ_6 into 50 intervals and C_6 into 120 intervals after trial-and-error inspection. A total of 6000 discrete states were defined.

We generated sample data from the BD simulations to build four MSMs for each of our four input levels: $\lambda = 0.2, 0.9, 2.0, 19.7$. For each model, BD simulations were initialized in different discrete states to cover a commonly visited region of the state space. The simulations were repeated to ensure that the important states have enough samples to account for stochastic effects. Simulations were conducted under both constant and time-varying inputs to enrich sampling, with voltage switching at intervals of $\Delta t = 100$ s, corresponding to the transition time used in the MSM. To preserve the Markovity of the system, a large transition time Δt is desired for better accuracy[66−68] but at the cost of intermediate information loss. After an investigation over a range of transition times on the model accuracy, the transition time $\Delta t = 100$ s was chosen to balance the MSM accuracy with the ability to actuate at useful time intervals (see main text for discussion of inherent system response time).

Markov Decision Process Based Optimal Control Policy Calculation. A Markov decision process (MDP) is composed of a MSM, a set t of discrete time epoch i, and a set A of discrete actions λ.[43,69] If t is a finite set, the MDP is called finite-horizon MDP, and it is called infinite-horizon MDP if t is an infinite set. An optimal control policy associated with an infinite-horizon MDP is a time-independent policy, that is, the control policy is stationary at each update interval. Considering the convenience in practical use as well as its ability for visualization and understanding, we investigated the infinite-horizon MDP based optimization problem to solve for a stationary optimal control policy. In the infinite-horizon MDP, the optimization is achieved over an infinite number of time steps, i, and the objective function is defined as

$$J^{\pi}(\mathbf{x}) = X\left\{ \sum_{i=0}^{\infty} \gamma^i R(\mathbf{x}_i, \lambda_i) \right\} \tag{15}$$

where X is the expectation operator, $\pi: S \rightarrow A$, is a feasible policy composed of control actions $\lambda_i \in A$, $\mathbf{x}_i \in S$ is the discrete state, i is the discrete time instant, and $\gamma \in (0,1)$ is the discount factor introduced to

ensure the convergence to optimality in dynamic programming. $R(\mathbf{x}_i, \lambda_i): S \times A \rightarrow \mathbf{R}$ is the one-stage reward function obtained when the system is in state $\mathbf{x}$, and a control action λ is taken. The optimal value function J^* and the optimal policy π^* are defined in eq 16, where "sup" indicates the supremum, and Π^s is the set of all feasible control policies,

$$J^*(\mathbf{x}) = \sup_{\pi \in \Pi^s} J^{\pi}(\mathbf{x}) \qquad \pi^*(\mathbf{x}) = \arg\left\{ \sup_{\pi \in \Pi^s} J^{\pi}(\mathbf{x}) \right\} = \arg J^*(\mathbf{x}) \tag{16}$$

In our particular calculation, the one-stage reward function is defined as $R(\mathbf{x}_i, \lambda_i) = \psi_6^2$, with a discount factor of $\gamma = 0.99$. With a discount factor so close to 1, the future values of the reward are nearly as important as the initial reward, over the ten control intervals considered here. The objective function was selected to achieve the highest possible ψ_6 value, which corresponds to a highly ordered, single domain crystalline state of the system. C_6 is not included explicitly in the objective function, but a high ψ_6 value state automatically requires a high C_6 value due to physical constraints. The optimal control policy was solved with dynamic programming in the MDP framework, using a policy iteration algorithm embedded in the MDP Toolbox from MATLAB central distribution.[70]

ASSOCIATED CONTENT

Ⓢ Supporting Information

The Supporting Information is available free of charge on the ACS Publications website at DOI: 10.1021/acsnano.6b02400.

> Additional materials and methods and simulation and analytical methods (PDF)
> Supplementary movie S1 (MOV)
> Supplementary movie S2 (MOV)

AUTHOR INFORMATION

Corresponding Authors
*E-mail: martha.grover@chbe.gatech.edu.
*E-mail: mabevan@jhu.edu.

Author Contributions
X.T., B.R., and Y.Y. contributed equally.

Notes
The authors declare no competing financial interest.

REFERENCES

(1) Ozbay, E. The Magical World of Photonic Metamaterials. *Opt. Photonics News* **2008**, *19*, 22−27.
(2) Stebe, K. J.; Lewandowski, E.; Ghosh, M. Oriented Assembly of Metamaterials. *Science* **2009**, *325*, 159−160.
(3) Arpin, K. A.; Mihi, A.; Johnson, H. T.; Baca, A. J.; Rogers, J. A.; Lewis, J. A.; Braun, P. V. Multidimensional Architectures for Functional Optical Devices. *Adv. Mater.* **2010**, *22*, 1084−1101.
(4) Engheta, N. 150 Years of Maxwell's Equations. *Science* **2015**, *349*, 136−137.
(5) Kalsin, A. M.; Fialkowski, M.; Paszewski, M.; Smoukov, S. K.; Bishop, K. J. M.; Grzybowski, B. A. Electrostatic Self-Assembly of Binary Nanoparticle Crystals with a Diamond-Like Lattice. *Science* **2006**, *312*, 420−424.
(6) Henzie, J.; Grünwald, M.; Widmer-Cooper, A.; Geissler, P. L.; Yang, P. Self-Assembly of Uniform Polyhedral Silver Nanocrystals into

Densest Packings and Exotic Superlattices. *Nat. Mater.* **2011**, *11*, 131−137.

(7) Nykypanchuk, D.; Maye, M. M.; van der Lelie, D.; Gang, O. DNA-Guided Crystallization of Colloidal Nanoparticles. *Nature* **2008**, *451*, 549−552.

(8) Shevchenko, E. V.; Talapin, D. V.; Kotov, N. A.; O'Brien, S.; Murray, C. B. Structural Diversity in Binary Nanoparticle Superlattices. *Nature* **2006**, *439*, 55−59.

(9) Macfarlane, R. J.; Lee, B.; Jones, M. R.; Harris, N.; Schatz, G. C.; Mirkin, C. A. Nanoparticle Superlattice Engineering with DNA. *Science* **2011**, *334*, 204−208.

(10) Cheng, Z.; Russel, W. B.; Chaikin, P. M. Controlled Growth of Hard-Sphere Colloidal Crystals. *Nature* **1999**, *401*, 893−895.

(11) Biancaniello, P. L.; Kim, A. J.; Crocker, J. C. Colloidal Interactions and Self Assembly Using DNA Hybridization. *Phys. Rev. Lett.* **2005**, *94*, 058302.

(12) Savage, J. R.; Blair, D. W.; Levine, A. J.; Guyer, R. A.; Dinsmore, A. D. Imaging the Sublimation Dynamics of Colloidal Crystallites. *Science* **2006**, *314*, 795−798.

(13) Yan, J.; Bloom, M.; Bae, S. C.; Luijten, E.; Granick, S. Linking Synchronization to Self-Assembly Using Magnetic Janus Colloids. *Nature* **2012**, *491*, 578−581.

(14) Koenig, G. M.; Lin, I.-H.; Abbott, N. L. Chemoresponsive Assemblies of Microparticles at Liquid Crystalline Interfaces. *Proc. Natl. Acad. Sci. U. S. A.* **2010**, *107*, 3998−4003.

(15) Soyka, F.; Zvyagolskaya, O.; Hertlein, C.; Helden, L.; Bechinger, C. Critical Casimir Forces in Colloidal Suspensions on Chemically Patterned Surfaces. *Phys. Rev. Lett.* **2008**, *101*, 208301.

(16) Swan, J. W.; Vasquez, P. A.; Whitson, P. A.; Fincke, E. M.; Wakata, K.; Magnus, S. H.; Winne, F. D.; Barratt, M. R.; Agui, J. H.; Green, R. D.; Hall, N. R.; Bohman, D. Y.; Bunnell, C. T.; Gast, A. P.; Furst, E. M. Multi-Scale Kinetics of a Field-Directed Colloidal Phase Transition. *Proc. Natl. Acad. Sci. U. S. A.* **2012**, *109*, 16023−16028.

(17) Kim, Y.; Shah, A. A.; Solomon, M. J. Spatially and Temporally Reconfigurable Assembly of Colloidal Crystals. *Nat. Commun.* **2014**, *5*, 3676.

(18) Armani, M. D.; Chaudhary, S. V.; Probst, R.; Shapiro, B. Using Feedback Control of Microflows to Independently Steer Multiple Particles. *J. Microelectromech. Syst.* **2006**, *15*, 945−956.

(19) Juarez, J. J.; Bevan, M. A. Feedback Controlled Colloidal Self-Assembly. *Adv. Funct. Mater.* **2012**, *22*, 3833−3839.

(20) Vezirov, T. A.; Gerloff, S.; Klapp, S. H. L. Manipulating Shear-Induced Non-Equilibrium Transitions in Colloidal Films by Feedback Control. *Soft Matter* **2015**, *11*, 406−413.

(21) Solis, E. O. P.; Barton, P. I.; Stephanopoulos, G. Controlled Formation of Nanostructures with Desired Geometries. 2. Robust Dynamic Paths. *Ind. Eng. Chem. Res.* **2010**, *49*, 7746−7757.

(22) Klotsa, D.; Jack, R. L. Controlling Crystal Self-Assembly Using a Real-Time Feedback Scheme. *J. Chem. Phys.* **2013**, *138*, 094502.

(23) Branduardi, D.; Gervasio, F. L.; Parrinello, M. From A to B in Free Energy Space. *J. Chem. Phys.* **2007**, *126*, 054103.

(24) Gast, A. P.; Russel, W. B. Simple Ordering in Complex Fluids - Colloidal Particles Suspended in Solution Provide Intriguing Models for Studying Phase Transitions. *Phys. Today* **1998**, *51*, 24−30.

(25) Anderson, V. J.; Lekkerkerker, H. N. W. Insights into phase transition kinetics from colloid science. *Nature* **2002**, *416*, 811−815.

(26) Poon, W. Colloids as Big Atoms. *Science* **2004**, *304*, 830−831.

(27) Pusey, P. N.; van Megen, W. Phase Behaviour of Concentrated Suspensions of Nearly Hard Colloidal Spheres. *Nature* **1986**, *320*, 340−342.

(28) Gasser, U.; Weeks, E. R.; Schofield, A.; Pusey, P. N.; Weitz, D. A. Real-Space Imaging of Nucleation and Growth in Colloidal Crystallization. *Science* **2001**, *292*, 258−262.

(29) Pertsinidis, A.; Ling, X. S. Diffusion of Point Defects in Two-Dimensional Colloidal Crystals. *Nature* **2001**, *413*, 147−150.

(30) Schall, P.; Cohen, I.; Weitz, D. A.; Spaepen, F. Visualization of Dislocation Dynamics in Colloidal Crystals. *Science* **2004**, *305*, 1944−1948.

(31) Alsayed, A. M.; Islam, M. F.; Zhang, J.; Collings, P. J.; Yodh, A. G. Premelting at Defects Within Bulk Colloidal Crystals. *Science* **2005**, *309*, 1207−1210.

(32) Ackerson, B. J.; Clark, N. A. Shear-Induced Partial Tranlational Ordering of a Colloidal Solid. *Phys. Rev. A: At., Mol., Opt. Phys.* **1984**, *30*, 906−918.

(33) Lumsdon, S. O.; Kaler, E. W.; Velev, O. D. Two-Dimensional Crystallization of Microspheres by a Coplanar AC Electric Field. *Langmuir* **2004**, *20*, 2108−2116.

(34) Goldenberg, L. M.; Wagner, J.; Stumpe, J.; Paulke, B.-R.; Görnitz, E. Simple Method for the Preparation of Colloidal Particle Monolayers at the Water/Alkane Interface. *Langmuir* **2002**, *18*, 5627−5629.

(35) Schermelleh, L.; Heintzmann, R.; Leonhardt, H. A Guide to Super-Resolution Fluorescence Microscopy. *J. Cell Biol.* **2010**, *190*, 165−175.

(36) Leung, B. O.; Chou, K. C. Review of Super-Resolution Fluorescence Microscopy for Biology. *Appl. Spectrosc.* **2011**, *65*, 967−980.

(37) Chen, Q.; Smith, J. M.; Park, J.; Kim, K.; Ho, D.; Rasool, H. I.; Zettl, A.; Alivisatos, A. P. 3D Motion of DNA-Au Nanoconjugates in Graphene Liquid Cell Electron Microscopy. *Nano Lett.* **2013**, *13*, 4556−4561.

(38) Zheludev, N. I.; Kivshar, Y. S. From Metamaterials to Metadevices. *Nat. Mater.* **2012**, *11*, 917−924.

(39) Juarez, J. J.; Liu, B. G.; Cui, J.-Q.; Bevan, M. A. kT-Scale Colloidal Interactions in High-Frequency Inhomogeneous AC Electric Fields. II. Concentrated Ensembles. *Langmuir* **2011**, *27*, 9219−9226.

(40) Adriani, P. M.; Gast, A. P. A Microscopic Model of Electrorheology. *Phys. Fluids* **1988**, *31*, 2757−2768.

(41) Edwards, T. D.; Beltran-Villegas, D. J.; Bevan, M. A. Size Dependent Thermodynamics and Kinetics in Electric Field Mediated Colloidal Crystal Assembly. *Soft Matter* **2013**, *9*, 9208−9218.

(42) Edwards, T. D.; Yang, Y.; Beltran-Villegas, D. J.; Bevan, M. A. Colloidal Crystal Grain Boundary Formation and Motion. *Sci. Rep.* **2014**, *4*, 6132.

(43) Chang, H.; Fu, M.; Hu, J.; Marcu, S. *Simulation-Based Algorithms for Markov Decision Processes*; Springer-Verlag: New York, 2006.

(44) Bowman, G.; Pande, V. S.; Noe, F. *An Introduction to Markov State Models and Their Application to Long Timescale Molecular Simulation*; Springer: Dordrecht, the Netherlands, 2014.

(45) Puterman, M. L. *Markov Decision Processes: Discrete Stochastic Dynamic Programming*; John Wiley & Sons: New York, 2014.

(46) Zhang, H.; Srolovitz, D. J.; Douglas, J. F.; Warren, J. A. Characterization of Atomic Motion Governing Grain Boundary Migration. *Phys. Rev. B: Condens. Matter Mater. Phys.* **2006**, *74*, 115404.

(47) Skinner, T. O. E.; Aarts, D. G. A. L.; Dullens, R. P. A. Grain-Boundary Fluctuations in Two-Dimensional Colloidal Crystals. *Phys. Rev. Lett.* **2010**, *105*, 168301.

(48) Anekal, S.; Bevan, M. A. Self Diffusion in Sub-Monolayer Colloidal Fluids Near a Wall. *J. Chem. Phys.* **2006**, *125*, 034906.

(49) Goldman, A. J.; Cox, R. G.; Brenner, H. Slow Viscous Motion of a Sphere Parallel to a Plane Wall – I. Motion Through a Quiescent fluid. *Chem. Eng. Sci.* **1967**, *22*, 637−651.

(50) Yuste, S. B.; Santos, A. A Heuristic Radial-Distribution Function for Hard Disks. *J. Chem. Phys.* **1993**, *99*, 2020−2023.

(51) Nagamanasa, K. H.; Gokhale, S.; Ganapathy, R.; Sood, A. K. Confined Glassy Dynamics at Grain Boundaries in Colloidal Crystals. *Proc. Natl. Acad. Sci. U. S. A.* **2011**, *108*, 11323−11326.

(52) Zhang, H.; Srolovitz, D. J.; Douglas, J. F.; Warren, J. A. Grain Boundaries Exhibit the Dynamics of Glass-Forming Liquids. *Proc. Natl. Acad. Sci. U. S. A.* **2009**, *106*, 7735−7740.

(53) Du, D.; Li, D.; Thakur, M.; Biswal, S. L. Generating an *in situ* Tunable Interaction Potential for Probing 2-D Colloidal Phase Behavior. *Soft Matter* **2013**, *9*, 6867−6875.

(54) Fernandes, G. E.; Beltran-Villegas, D. J.; Bevan, M. A. Interfacial Colloidal Crystallization *via* Tunable Hydrogel Depletants. *Langmuir* **2008**, *24*, 10776−10785.

(55) Lee, W.; Chan, A.; Bevan, M. A.; Lewis, J. A.; Braun, P. V. Nanoparticle-Mediated Epitaxial Assembly of Colloidal Crystals on Patterned Substrates. *Langmuir* **2004**, *20*, 5262−5270.

(56) Ferraro, M. E.; Bonnecaze, R. T.; Truskett, T. M. Graphoepitaxy for Pattern Multiplication of Nanoparticle Monolayers. *Phys. Rev. Lett.* **2014**, *113*, 085503.

(57) Edwards, T. D.; Yang, Y.; Everett, W. N.; Bevan, M. A. Reconfigurable Multi-Scale Colloidal Assembly on Excluded Volume Patterns. *Sci. Rep.* **2015**, *5*, 13612.

(58) Bahukudumbi, P.; Everett, W. N.; Beskok, A.; Huff, G. H.; Lagoudas, D.; Ounaies, Z.; Bevan, M. A. Colloidal Microstructures, Transport, and Impedance Properties within Interfacial Micro-electrodes. *Appl. Phys. Lett.* **2007**, *90*, 224102.

(59) Juarez, J. J.; Feicht, S. E.; Bevan, M. A. Electric Field Mediated Assembly of Three Dimensional Equilibrium Colloidal Crystals. *Soft Matter* **2012**, *8*, 94−103.

(60) Beckham, R. E.; Bevan, M. A. Interfacial Colloidal Sedimentation Equilibrium I. Intensity Based Confocal Microscopy. *J. Chem. Phys.* **2007**, *127*, 164708.

(61) Beltran-Villegas, D. J.; Schultz, B. A.; Nguyen, N. H. P.; Glotzer, S. C.; Larson, R. G. Phase behavior of Janus colloids determined by sedimentation equilibrium. *Soft Matter* **2014**, *10*, 4593−4602.

(62) Liberek, K.; Lewandowska, A.; Ziętkiewicz, S. Chaperones in Control of Protein Disaggregation. *EMBO J.* **2008**, *27*, 328−335.

(63) Fernandes, G. E.; Beltran-Villegas, D. J.; Bevan, M. A. Spatially Controlled Reversible Colloidal Self-Assembly. *J. Chem. Phys.* **2009**, *131*, 134705.

(64) Nelson, D. R.; Halperin, B. I. Dislocation-Mediated Melting in Two Dimensions. *Phys. Rev. B: Condens. Matter Mater. Phys.* **1979**, *19*, 2457−2484.

(65) Rein ten Wolde, P.; Ruiz-Montero, M. J.; Frenkel, D. Numerical Calculation of the Rate of Crystal Nucleation in a Lennard-Jones System at Moderate Undercooling. *J. Chem. Phys.* **1996**, *104*, 9932.

(66) Sarich, M.; Noé, F.; Schütte, C. On the Approximation Quality of Markov State Models. *Multiscale Model. Simul.* **2010**, *8*, 1154−1177.

(67) Prinz, J.-H.; Wu, H.; Sarich, M.; Keller, B.; Senne, M.; Held, M.; Chodera, J. D.; Schütte, C.; Noé, F. Markov Models of Molecular Kinetics: Generation and Validation. *J. Chem. Phys.* **2011**, *134*, 174105.

(68) Pande, V. S.; Beauchamp, K.; Bowman, G. R. Everything You Wanted to Know About Markov State Models but Were Afraid to Ask. *Methods* **2010**, *52*, 99−105.

(69) Bertsekas, D. P. *Dynamic Programming and Optimal Control*, 3rd ed.; Athena Scientific: Nashua, NH, 2012.

(70) Chadès, I.; Cros, M.; Garcia, F.; Sabbadin, R. Markov Decision Processes (MDP) Toolbox. https://www.mathworks.com/matlabcentral/fileexchange/25786-markov-decision-processes--mdp--toolbox.